Journal of The Electrochemical Society, 2020 **167** 124520

Towards a Harmonized Accelerated Stress Test Protocol for Fuel Starvation Induced Cell Reversal Events in PEM Fuel Cells: The Effect of Pulse Duration

Robert Marić,[1,2,*] Christian Gebauer,[1] Markus Nesselberger,[1] Frédéric Hasché,[3,,z] and Peter Strasser[2,**,z]**

[1]*Hydrogen Systems, Heraeus Deutschland GmbH & Co. KG, Hanau 63450, Germany*
[2]*Electrochemical Catalysis, Energy, and Materials Science Laboratory, Technische Universität Berlin, Berlin 10623, Germany*
[3]*Institute of Technical Chemistry, Technical Electrocatalysis Laboratory, Technische Universität Braunschweig, Braunschweig 38106, Germany*

Global fuel starvation is an undesired event during fuel cell operation that results in serious degradations at the anode catalyst layer caused by the concomitant reversal of the cell potentials. Several groups have therefore intensified their research efforts towards the implementation of suitable diagnostic tools and accelerated stress test (AST) protocols that mimic cell reversal events. However, the current number of different test protocols requires consolidation and harmonization to define durability targets towards cell reversal tolerance and to benchmark newly developed materials. To create a basis for harmonization, this study examines the difference between pulsed and quasi-continuous AST protocols at the catalyst-coated membrane level. Utilizing a single-cell setup combined with an on-line mass spectrometer, a 2.5-fold increase in the carbon corrosion rates were found for short-pulsed compared to long-lasting cell reversal events. The enhanced corrosion was associated with a 2.2-fold higher loss of electrochemically active surface area and a 15% higher reduction in anode catalyst layer thickness. By contrast, the overall cell performance decreased additionally by 40–50 mV for samples under long-lasting cell reversal events. The decay is mainly driven by an increased ohmic resistance, presumably originating from a more pronounced surface oxide formation on the carbon support.
 [DOI: 10.1149/1945-7111/abad68]

Manuscript submitted June 4, 2020; revised manuscript received July 7, 2020. Published August 25, 2020.

Supplementary material for this article is available online

The reduction of the total cost of a proton exchange membrane hydrogen fuel cell (PEMFC) system requires the identification of cost saving potentials of all individual components, such as bipolar plates, catalyst-coated membranes or gas diffusion materials. At the catalyst-coated membrane (CCM) level, the increase in the performance and/or durability continues to be a promising material-specific strategy. Durable CCMs need to withstand a number of different challenging operating conditions, such as load cycling, open cell voltage operation, start-up/shut-down events, sub-freezing conditions, temperature and relative humidity variations, air and fuel impurities, and, last but not least, air and fuel starvation events.[1]

In this context, global fuel starvation is an undesired event during fuel cell operation that results in serious and irreversible degradations at the anode catalyst layer caused by the concomitant reversal of the cell potentials. As a result of this, corrosion of the carbon-based catalyst support materials such as Vulcan or other high surface-area carbons ensues.[2] As a consequence, the PEMFC performance decreases due to the collapse of the electrode pore structure, increased contact resistances, loss of hydrophobicity, damaged catalyst particle connectivity and increased catalyst particle size.[3–5] In case of fuel starvation, the proton and electron supply based on the hydrogen oxidation reaction (HOR) cannot be sustained due to insufficient fuel supply. However, in a galvanostatically operating stack - with multiple cells connected in series - individual cells suffering from fuel starvation will be forced to sustain the global electric current to and from neighboring cells that operate smoothly.[1] To compensate the current demand, the anode potential rises to levels where water electrolysis (*oxygen evolution reaction*, OER, Eq. 1) and corrosion of the carbon-based components (*carbon oxidation reaction*, COR, Eq. 2) take place instead:

$$2H_2O \rightarrow O_2 + 4H^+ + 4e^-(E_0 = 1.23\ V_{RHE}) \quad [1]$$

$$C + 2H_2O \rightarrow CO_2 + 4H^+ + 4e^-(E_0 = 0.21\ V_{RHE}) \quad [2]$$

While thermodynamically carbon corrosion (Eq. 2) could start at much lower potentials compared to water electrolysis (Eq. 1), the kinetic barriers of this reaction make significant corrosion currents possible only at potentials above 1.0 V_{RHE}.[6] The increase in anode potential finally leads to the overall cell voltage being reversed compared to normal operation.[7] The high potentials cause severe damage to the widely employed carbon-supported anode catalysts and reduce the overall cell performance within few seconds[8] under fuel-starved conditions and in absence of suitable mitigation strategies. As the industry is heading towards ultra-low Pt loaded anodes, the anode becomes increasingly sensitive to minimal disturbances. The effective development of cell reversal-tolerant anode materials requires suitable simulated fuel starvation conditions and on-line diagnostics that help understand the molecular origins and mechanistic details of the materials degradation.

In the literature, a number of different phenomena were linked to cell reversal, e.g. insufficient fuel supply due to blocked flow field channels by water or ice; other causes included blocked pathways across gas diffusion layers and across active catalyst layer pores as well as poor fuel regulation during sudden load changes and start-ups.[7,9] In addition, the operation of a fuel cell stack close to unity fuel stoichiometry or running the anode compartment in so called dead-end mode,[10,11] with the aim of raising the system's efficiency, exacerbated the imbalance between fuel supply and demand even more. Thus, strict requirements are imposed on the control systems. Possible ways to detect cell reversal occurrence are to either monitor the voltage of individual or blocks of cells,[12] or to analyze the exhaust gas composition. Affected cells could then be switched off individually by diodes or the entire stack could be shut down to prevent serious irreversible damage.[1,9] Also, a feedback control of the fuel volumetric flow rates and pressures toward higher

*Electrochemical Society Student Member.
**Electrochemical Society Member.
[z]E-mail: f.hasche@tu-braunschweig.de; pstrasser@tu-berlin.de

values is feasible. However, these system mitigation strategies[13] are complex and expensive, or, in the latter case, may take a while to take effect until normal fuel cell operation is restored.

Therefore, in the scientific and patent literature various strategies for the development of cell reversal tolerant anode materials are described, aiming to increase the intrinsic stability of the anode catalyst layer against fuel starvation conditions. These include the incorporation of a second catalyst component with a significantly enhanced OER activity,[3,14–19] an anode catalyst with concurrent activity towards HOR and OER,[20–22] more corrosion-resistant catalyst supports,[14,23] non-carbon supports,[8,24–26] support materials exhibiting a hydrogen spillover effect,[27] sacrificial materials,[28] hydrophobic additives[29] or a combination of those.

To demonstrate the efficacy of newly-developed cell reversal-tolerant anode materials or to study the degradation mechanisms during fuel starvation,[14,15,30] various cell reversal test protocols have been used by different researchers in academia and industry alike in single cell[14,20,31] or short stack configuration.[16] Among those, the most common way to mimic gross fuel starvation conditions is to exchange the anode hydrogen gas flow with an inert gas, e.g. N_2 or Ar,[14,20,31] or sub-stoichiometric H_2,[7,32,33] while maintaining a constant current density from an external source. The test is terminated, when a certain time under fuel starvation conditions is achieved or the cell potential reaches a pre-defined cut-off voltage, e.g. −2.0 V, where membrane breakthrough becomes likely to occur.[7] Further methods include the repetition of the above-mentioned test with interim recovery phases in normal fuel cell mode (H_2/Air gas supply for anode and cathode, respectively) and the measurement of a polarization curve in between, until a certain voltage loss is reached.[3,15,30,34] Also, short cell reversal pulses were often reported, using either pulse-like switching of the anode gas between H_2 (normal fuel cell mode) and an inert gas[34] or sub-stoichiometric H_2[5,35] (cell reversal mode), or using cell voltage cycling between 0 and > 1.0 V in the N_2/H_2 gas mode.[24]

The large number of different test protocols makes it difficult to evaluate and compare the effectiveness and improvements made by the various groups working on cell reversal tolerant anode materials. Moreover, feasibility studies under application-oriented conditions are necessary to get a deeper understanding on the failure mechanism under real-life-operation and the interaction of system and material mitigation strategies.

Harmonizing test protocols and identifying application-oriented conditions would allow the definition of requirements and specifications for the selection of appropriate anode materials. In order to create a wide data basis for future decisions regarding accelerated stress test protocols, the present study aims to evaluate the difference between the application of continuous versus pulsed cell reversal protocols and their impact on degradation of catalyst-coated membranes. The pulsed protocol is to represent the case where system mitigation strategies, such as voltage monitoring and adaptable flow rates, are applied in order to minimize the time under fuel starved conditions. By contrast, the continuous protocol is to represent the system operation case in absence of system-level remedies to avoid fuel starvation conditions.

To assess the degradation progress during the application of the different test protocols with varying pulse durations, carbon corrosion rates are quantified utilizing on-line mass spectrometry. Further, recent electrochemical and physical characterization methods are used in order to investigate the origin of the various voltage loss contributions that cause a performance decay due to progressive electrode degradation. As will be shown in detail, the results indicate that short pulsed cell reversal events cause greater catalyst degradation in terms of carbon support corrosion and catalyst surface area loss compared to long-lasting cell reversal events. On the other hand, a significant deterioration of the ohmic resistance of stress tested catalyst-coated membranes - situated under long-lasting cell reversal events - induces an additional voltage loss to the overall cell performance.

Experimental

The accelerated stress test (AST) protocol includes the variation of five different pulse durations of a single cell reversal event, ranging from short to long-lasting pulses. Therefore, five similar produced catalyst-coated membranes in single cell setup (50 cm^2_{geo}) were tested. An appropriate number of cell reversal pulses were repetitively applied until an accumulated time under fuel starvation conditions was reached, e.g. 900 s. To investigate the differences between the applied AST protocols on the degradation of the membrane electrode assemblies (MEAs), an on-line mass spectrometry was utilized along with interim electrochemical performance characterization (after 300, 600 and 900 s of accumulated cell reversal time) as well as a post-mortem catalyst layer thickness measurement via scanning electron microscopy.

Materials and hardware setup.—An in-house made high surface area platinum catalyst (40 wt% metal loading) on a carbon carrier (commercially available medium surface area carbon material, Vulcan XC72R, Cabot Corporation) (Pt/C) was used both as anode and cathode catalyst layer. To enhance cell reversal tolerance an in-house made OER-active catalyst (IrO_2) was mixed into the anode catalyst layer with an iridium metal content in the final catalyst layer of 25 wt% with respect to the platinum catalyst layer loading. An ink was formulated (ionomer to carbon weight ratio, I/C = 1) using low-boiling solvents and a Nafion® ionomer (D2020, The Chemours Company). The catalyst layers were prepared by the well described decal transfer technique[36] including a hot-pressing step of the bar-coated electrodes onto a commercially available membrane (Gore M820.15, W. L. Gore & Associates, Inc.). Five similar CCMs were produced with platinum loadings of 0.1/0.4 mg_{Pt} cm^{-2}_{geo} (anode/cathode). Each CCM was sandwiched between two gas diffusion layers (GDL, Sigracet 28BC, SGL Carbon GmbH) to form the MEA. A GDL compression of approximately 20% was adjusted by using fiberglass reinforced PTFE gaskets (Fiberflon GmbH). The electrochemical characterizations were carried out in single cell configuration (50 cm^2_{geo} active area) using a multi-channel serpentine graphite flow field[37] in counter-flow mode on a G60 test bench (Greenlight Innovation Corp.). The CO_2 and O_2 contents were quantified with a Cirrus 3-XD quadrupole mass spectrometer (MS) (MKS instruments Deutschland GmbH). The gas sample to be analyzed has been taken via a stainless-steel capillary that was heated up to 150 °C and connected via a T-piece to the anode exhaust gas pipe. To avoid condensation of water, the anode exhaust pipe and all connections between the cell hardware and MS were appropriately insulated and heated to 140 °C with a heating tape (HORST GmbH), following the well described experimental setup of Mittermeier et al.[38]

MEA pre-tests.—Prior to the start of the electrochemical experiments several commonly used pre-tests are conducted at ambient temperature to detect unwanted gas leaks at gaskets and connected hoses, electrical shorting or membrane pinholes.[36]

MEA conditioning and performance characterization.—Subsequently, all MEAs in this study were conditioned under pressurized and humidified H_2/Air (anode/cathode) with flow rates of 1400/3300 nccm, pressures of 150 $kPa_{abs,inlet}$ and 60 °C cell and dew point temperatures (relative humidity, RH = 100%). The conditioning procedure consists out of eight consecutive potentiostatic cycles with the following partial steps: (i) 0.60 V for 45 min, (ii) 0.95 V for 5 min, and (iii) 0.85 V for 10 min. After finishing the conditioning procedure, the initial polarization curve was measured. Cell temperature and dew point of 80 °C with fully humidified H_2/Air (RH = 100%), differential flow rates of 1000/5000 nccm and a pressure of 150 $kPa_{abs,inlet}$ at both electrodes. The current-voltage curve was measured galvanostatically by varying an adjustable load. Each current step was held for > 5 min before averaging the last 30 s of the measured voltage. Subsequently, the

high frequency resistance (HFR)[39] was determined at each DC current step utilizing electrochemical impedance spectroscopy (EIS) in pseudo-galvanostatic mode within a frequency range of 100 kHz - 0.01 Hz and an AC perturbation of 4 mV_{rms}. The HFR is evaluated from the high frequency *x*-axis intercept (imaginary part = 0) of the impedance spectra in the respective Nyquist plot.

Electrochemically active surface area.—Cyclic voltammograms (CVs) were measured at 35 °C with fully humidified gases (RH = 100%) at ambient pressures. Three CVs were measured between 0.07–1.05 V_{RHE} at scan rates of 20, 50 and 100 mV s^{-1}. For the cathode CVs, the anode side was exposed to 200 nccm H_2, whereas 50 nccm N_2 (1 nccm cm_{geo}^{-2}) was supplied to the cathode side.[40] Directly afterwards the anode CVs were measured. Therefore, the cathode side was exposed to 1000 nccm 3% H_2 in Ar, whereas 50 nccm N_2 was supplied to the anode side. The data shown were evaluated based on the 50 mV s^{-1} scans. The electrochemically active surface area (ECSA) was calculated from the charge of underpotentially deposited hydrogen (H_{upd}) and 210 μC cm_{Pt}^{-2} for polycrystalline platinum.[41] Note that the lower potential limits of the CVs were corrected by the partial pressure dependent term of the Nernst equation if diluted instead of pure H_2 was used (approx. 47 mV for 3% H_2 at 35 °C).

Anode exhaust gas analysis.—Prior to the analysis of the anode exhaust gas, the ion signal intensities were calibrated for the mass-to-charge ratios (m/z) of interest, i.e. m/z = 44 for CO_2 and m/z = 32 for O_2. The calibration procedure (steps *I–IV*, described below) was carried out after cell pre-conditioning procedure and with the same conditions (temperature, pressure, flow rate) as adjusted for the cell reversal experiments. Details on calibration procedure and gas modes can be found in Fig. S1 (available online at stacks.iop.org/JES/167/124520/mmedia) in the supplemental material. *(I)* A zero-gas (air leak) calibration was performed with pure Ar on the anode side to account for traces of ambient air diffusing through leakages at gaskets and joints. *(II)* Afterwards the MS was calibrated with three premixed calibration gases (Nippon Gases Deutschland GmbH) of increasing CO_2 and O_2 contents (2000 ppm, 2% and 5%) in Ar carrier gas (grade 5.0). All measured ion currents were corrected by the first zero-gas (air leak) analysis from step *I* and normalized to the m/z = 40 base peak of the Ar carrier gas to form a multi-point calibration curve. Note that during the first zero-gas (air leak) and MS calibration the cathode was fed with fully humidified N_2 instead of air, in order to minimize the exposure time under oxidizing conditions, which happens due to long calibration times (~5 h) at open cell voltage (OCV) and repetitive changing gas fronts during the purging sequence (s. below).[42] *(III)* A second zero-gas (air permeation) calibration in Ar/Air gas mode was performed afterwards to remove all remaining CO_2 and O_2 from the calibration gases (<20 ppm). Further, this second zero-gas (air permeation) calibration was used to consider the air that permeates through the membrane from the cathode to the anode side during the actual fuel starvation experiment, which would otherwise lead to an over-estimation of the measured O_2. *(IV)* After the second zero-gas (air permeation) calibration, Ar was replaced by H_2 for the subsequent cell reversal experiment. Following the calibration procedure of Mittermeier et al.[38] a purging sequence was applied between each gas exchange for ~25 min in order to remove the former gas (Table I). The ion currents measured during the cell reversal test were corrected by the second zero-gas (air permeation) calibration from step *III*, normalized to the m/z = 40 base peak and analyzed by applying the above obtained linear calibration curve.

Anode potential measurement.—A hydrogen reference electrode was implemented in order to investigate the individual anode potentials during the cell reversal experiment. For this reason, a 10 cm_{geo}^2 active area of the same electrode coating as used for the cathode side was hot-pressed onto a membrane (Gore M820.15, W. L. Gore & Associates, Inc.). This reference electrode was assembled into the Flex-Stack cell hardware (Fuel Cell Store) with a gas diffusion layer (GDL, Sigracet 28BC, SGL Carbon GmbH) attached. Following the study by Hu et al.[31] a membrane strip of the reference electrode—acting as an ionic bridge—was connected to the membrane of the actual MEA of interest. Note that a misalignment factor of approx. 4[43] was achieved by hot-pressing the anode of the MEA of interest with a small offset towards the cathode. The potential was measured at the overhanging edge. To achieve a stable reference electrode, the exposed membrane strip was kept as short as possible and well hydrated by wrapping a moist Multitex® Z47 cloth around.[44] One end of the cloth was placed into a beaker containing high-purity water. Throughout the cell reversal experiments the reference electrode was supplied with 4% H_2 in N_2 at room temperature. The measured potential between the anode and reference electrode was corrected by the partial pressure and temperature dependent term of the Nernst equation with respect to 100 $kPa_{abs,inlet}$ H_2 and 25 °C (approx. 41 mV for 4% H_2 at 25 °C).

Cell reversal experiments.—Cell reversal experiments were performed at 80 °C cell temperature and dew points (RH = 100%), 150 $kPa_{abs,inlet}$ pressure (both sides) and 1000/5000 nccm flow rates (anode/cathode). During the whole cell reversal experiment a constant current of 0.2 A cm_{geo}^{-2} was applied (Reference 30k Booster, Gamry Instruments, Inc.). Prior to each accelerated stress test procedure the cell was operated in H_2/Air mode for 10 min. In order to mimic normal operation mode and fuel starvation conditions, the anode gas was alternated between H_2 and Ar (shaded colors in Fig. 1), while the cathode was continuously supplied with air. A constant Ar flow was maintained throughout the cell reversal event to prevent a "vacuum effect"[33,45] which would result in gas (ambient air/H_2 mixture) being drawn into the cell from the exhaust line. A similar experimental setup as previously reported for start-up/shut-down investigations[46] was used here to ensure accurate and sharp H_2 to Ar and Ar to H_2 gas fronts as well as humidified gases during all partial steps of the test. Briefly, two constant gas streams with separate humidifiers for H_2 and Ar as well as four simultaneously switching valves, ensured constant pressures, flow rates and humidification levels during gas switching. The black line in Fig. 1 shows a typical cell voltage response during a cell reversal event. The pulse duration (t_{pulse}) of a single cell reversal event was varied in this study between 10, 37.5, 150, 300 and 900 s in order to simulate different exposure times under fuel starvation conditions on the five previously produced CCMs, ranging from short pulsed to continuous cell reversal sequences. The t_{pulse} is defined as the time interval at which the overall cell voltage is permanently below 0 V within one cell reversal event, i.e. one gas exchange from H_2 filled anode to Ar filled anode and vice versa. Between each cell reversal pulse, 4 min in H_2/Air mode was set in order to simulate normal operating conditions and to let the MS signals subside to the

Table I. Applied purging sequence for the gas exchange between the different gases used for the zero-gas analysis and calibration procedure. The set values of the gas flow rates have been adjusted (cf.[38]) to lie in between the maximum flow rates of our mass flow controllers connected in parallel (100, 750, 2000 nccm) in order to ensure a proper removal of the former gas from the gas pipes and humidifier.

Step	1	2	3	4	5	6	7	8	9	10	11
Gas flow rate/nccm	100	500	1000	500	100	1000	500	100	1000	500	1000
Dwell time/s	60	300	300	60	60	60	60	60	60	120	300

background level. An appropriate number of cell reversal events were repetitively applied to attain an accumulated cell reversal time (t_{accum}) of 300, 600 and 900 s. After t_{accum} = 300, 600 and 900 s a polarization curve as well as the ECSA of the cathode and anode were measured. In contrast to the t_{pulse}, the term t_{accum} refers to the total time in cell reversal mode, i.e. the number of all individual cell reversal events (n_{CR}) times a certain t_{pulse} (Eq. 3).

$$t_{accum} = \sum_{i=1}^{n_{CR}} t_{pulse} = n_{CR} * t_{pulse} \quad [3]$$

Catalyst layer thicknesses measurement.—After the electrochemical experiments, an approximately 4 cm^2 cutout of the MEA was taken from the inlet, middle and outlet region, respectively, in order to determine the catalyst layer thicknesses of either a fresh (beginning of life, BOL) or a degraded MEA, e.g. after t_{accum} = 900 s, also denoted as end of life (EOL). The cutouts were embedded into a polymer resin (EpoFIX Resin, Struers GmbH). After the material had cured, the specimen was ground on abrasive paper (SiC, Struers GmbH) and polished on polishing cloth (MD Dur/MD Mol, Struers GmbH) with diamond spray (Cloeren Technology GmbH) and water-based lubricant (Cloeren Technology GmbH) in lateral and longitudinal direction to the flow field channels. The catalyst layer thicknesses were obtained at 54 individual measuring points evenly distributed over the MEA cutout using a scanning electron microscope (SEM) JSM-IT100 (JEOL GmbH) in backscattering mode with an acceleration voltage of 20 kV and a working distance of 10 mm. The mean value and the 95% confidence interval (CI) were then calculated from the individual values to make reliable statements on the evolution of the catalyst layer thicknesses throughout the variation of t_{pulse}.

Results and Discussion

Figure 2 shows the flow chart of the general accelerated stress test protocol for induced cell reversal events caused by fuel starvation, which were used in this study. Prior to the induced cell reversal tests, various MEA pre-tests and conditioning as well as calibration steps were performed, as described in the experimental section. The performance of the MEAs was characterized initially as well as intermittently during the tests, whenever t_{accum} equaled to 300 s. Table II shows the beginning of life (BOL, t_{accum} = 0) cell voltage (V_{cell}) at 1.0 A cm^{-2}_{geo} as well as the voltage loss (ΔV_{loss}) with progressing accumulated cell reversal time, t_{accum}, for different pulse durations (t_{pulse}). Note, the full polarization curves can be found in Fig. S2 in the supplemental material. For comparison, the voltage losses in the kinetic region were quite comparable and ranged from 10 ± 2 mV at 0.1 A cm^{-2}_{geo} for MEAs of t_{pulse} = 10–300 s to 15 mV for t_{pulse} = 900 s (not shown in Table II). A probable explanation and impact of this voltage loss could be attributed to an approx. 8% ECSA loss of the cathode and will be discussed in detail in the following sections. Turning to Table II, the BOL cell voltage at 1.0 A cm^{-2}_{geo} is approx. 639 ± 15 mV. With progressing t_{accum} the loss of performance increased and plateaued somewhat for the short

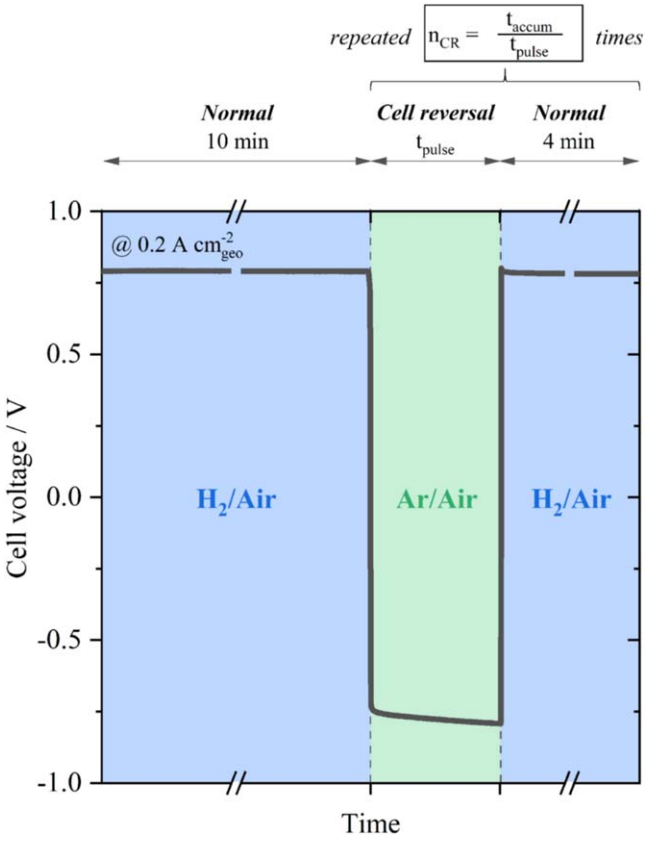

Figure 1. Representative overall cell voltage curve during accelerated stress test with induced cell reversal event. Individual colors illustrate the applied gas mode, H_2/Air: blue and Ar/Air: green during the procedure which was repeated several times (n_{CR}) until an accumulated cell reversal time (t_{accum}) of 900 s is reached. Constant current density of 0.2 A cm^{-2}_{geo} externally supplied, 80 °C cell temperature, RH of 100% for the supplied gases, 150/150 $kPa_{abs,inlet}$ total pressures and 1000/5000 nccm constant flow rates for the anode and cathode, respectively.

reversal pulses after t_{accum} = 300 s. After t_{accum} = 900 s, a cumulative voltage loss of 41–51 mV was found for the short-pulsed MEAs, i.e. t_{pulse} = 10 and 37.5 s. However, an additional 40–50 mV decrease in voltage was observed for the two samples with the largest t_{pulse}, i.e. 300 and 900 s.

During the cell reversal experiments, the anode exhaust gas was analyzed using on-line mass spectrometry. Figures 3a and 3b show the total molar amounts of CO_2 and O_2, respectively, which had accumulated at cell reversal time intervals of 300 s (t_{accum} = 300, 600, 900 s) as a function of the reversal pulse duration, t_{pulse}. In general, the shorter t_{pulse}, the more CO_2 was detected (Fig. 3a). The total amount of measured CO_2 over the entire test time increased non-linearly by a factor of 2.5x, when the fuel starvation pulses were

Table II. Beginning of life (BOL) cell voltage (V_{cell}) and voltage loss (ΔV_{loss}) at 1.0 A cm^{-2}_{geo} in dependence of the pulse duration (t_{pulse}) and accumulated cell reversal time (t_{accum}). The polarization curves were measured in H_2/Air at 80 °C with fully humidified gases (RH = 100%) at symmetrical pressures of 150 $kPa_{abs,inlet}$ and constant flow rates of 1000/5000 nccm for the anode and cathode, respectively. The voltage loss in the kinetic region is about 10 ± 2 mV at 0.1 A cm^{-2}_{geo} for MEAs of t_{pulse} = 10–300 s and 15 mV for t_{pulse} = 900 s (not shown).

t_{pulse}/s		10		37.5		150		300		900	
		V_{cell}	ΔV_{loss}	V_{cell}	ΔV_{loss}	V_{cell}	ΔV_{loss}	V_{cell}	ΔV_{loss}	V_{cell}	ΔV_{loss}
		mV		mV		mV		mV		mV	
t_{accum}/s	**0**	644	0	636	0	654	0	628	0	633	0
	300	603	41	599	37	624	30	615	13	—	—
	600	602	42	595	41	611	43	592	36	—	—
	900	591	53	595	41	590	64	541	87	540	93

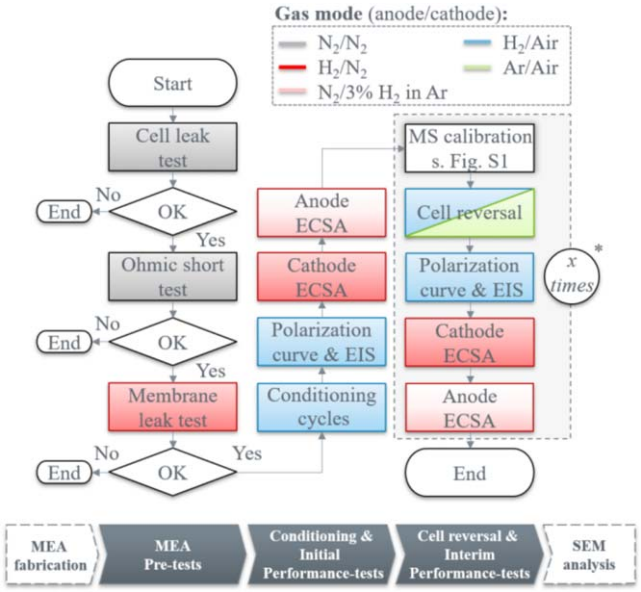

Figure 2. Flow chart of the accelerated stress test protocol for cell reversal events. The applied gas mode is indicated by the colored rectangles for each partial step of the testing sequence. Asterisk: The framed sequence is repeated three times for pulse durations (t_{pulse}) of 10, 37.5, 150 and 300 s, i.e. after an accumulated cell reversal time (t_{accum}) of 300 s, and one time for t_{pulse} = 900 s.

shortened from 900 to 10 s. For a better understanding of this behavior it is worth noting that the gas exchanges between H_2 and Ar during our fuel starvation phases trigger sharply changing anode potentials from 0 to > 1.4 V_{RHE} and vice versa, which increased in frequency with shorter t_{pulse} (see Fig. S3b). These findings of increasing CO_2-amounts with decreasing t_{pulse} - and thus a higher number of potential changes - agree with the observations made by Maass et al.,[6] confirming that corrosion rates in potentiodynamic mode are higher compared to constant potential operation. They observed a rise of the corrosion rate during their potential scans in the range of 0.4–0.9 V_{RHE}, a lower onset potential for carbon corrosion as well as higher absolute corrosion rates in the vicinity of a Pt-catalyst compared to pure carbon electrodes. From a mechanistic point of view,[6,47,48] it was suggested that adsorbed water or hydroxyl groups on Pt act as reaction intermediates during the carbon corrosion, starting at defect sites. Also, a substantial dependence of the carbon corrosion on the lower and upper potential limits was observed in their studies, indicating that the catalytic activity of Pt is lowered by the formation of a passivating oxide layer on the catalyst particles if the catalyst is not reduced at potentials < 1.0 V in the meantime. Further it was shown that hydrogen peroxide formation leads to increased carbon corrosion at low potentials < 0.2 V, regardless of the vicinity of a Pt-catalyst.[6,48] Notably, a lowered carbon corrosion on aged Pt/C-electrodes was found,[6] which is in good agreement with the diminishing CO_2-amount in the anode exhaust gas stream with progressing cell reversal time in our study (see Fig. 3a), i.e. increasing t_{accum} from 0–300 > 300–600 > 600–900 s. Beyond the role of Pt in the carbon corrosion pathways, a study on pure carbon electrodes by Ashton et al.[49] suggested a passivation of the carbon surface at high potentials (> 1.0 V_{RHE}) by the formation of oxygen-based non-electrochemically oxidizable functional groups which inhibit further carbon corrosion. However, the corrosion process was found to be re-initialized by the reduction of the passivated carbon surface at potentials lower than 0.24 V_{RHE}. Nevertheless, their results are a complementary explanation for our findings of higher CO_2-amounts measured for the shortest pulsed fuel starvation experiments.

Figure 3b shows that, except for the shortest pulse time, the amount of measured O_2 in the anode exhaust dropped only slightly with decreasing t_{pulse}, while the detected oxygen at progressing t_{accum} intervals remained essentially constant, which leads to the conclusion that the efficiency of the added OER catalyst remains unchanged over the testing time. A sudden steeper drop in the oxygen amount was observed for t_{pulse} = 10 s. Note that after a H_2 to Ar gas exchange is initiated, the H_2 content in the anode gradually decreases. Hence, the gas exchange could have been incomplete for the short cell reversal pulses (t_{pulse} = 10 and 37.5 s). Indeed, a relatively large m/z = 2 signal (assigned to H_2), more specifically 80% and 50% signal height between upper signal level in H_2/Air mode (100%) and background level in Ar/Air mode (0%), was still

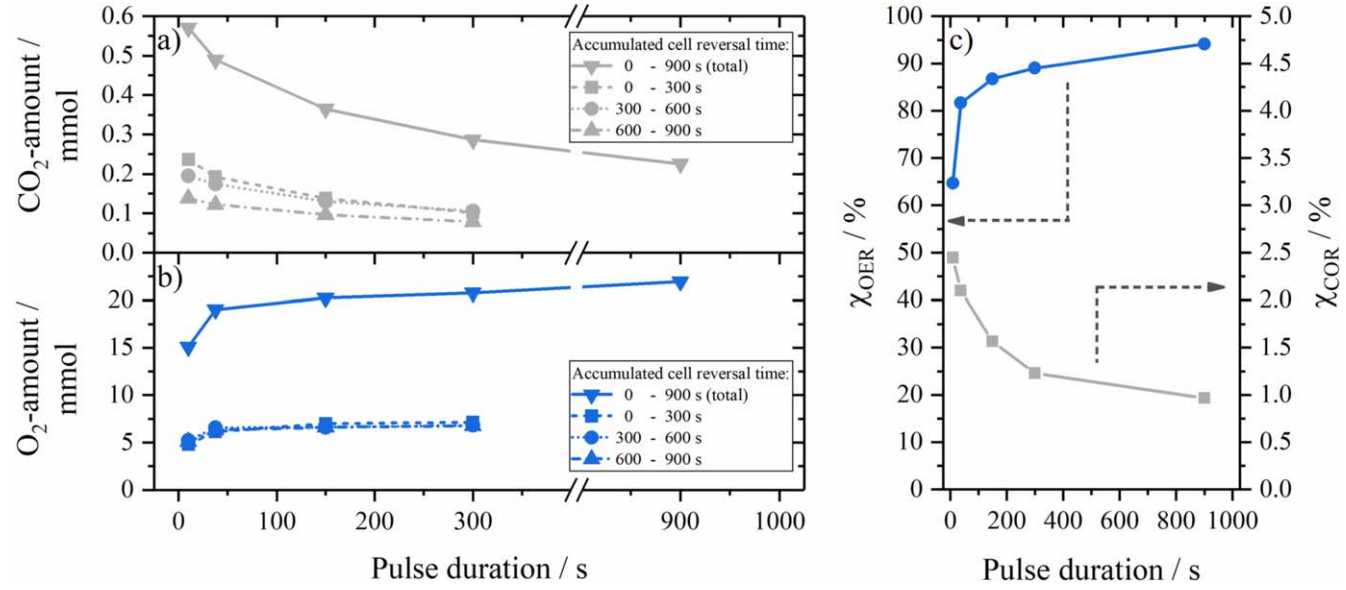

Figure 3. Detected amount of CO_2 and O_2 anode exhaust gas in dependence of the applied pulse duration during accelerated stress test protocol for cell reversal experiments. (a) Detected CO_2− and (b) O_2− amount during various time intervalls. (c) Current efficiencies of the oxygen evolution reaction (χ_{OER}) and the carbon oxidation reaction (χ_{COR}) as a function of the pulse duration. Assuming Faraday's law and a 4-electron process according to Eqs. 1 and 2, the OER and COR currents were calculated from MS results and normalized to the externally applied current of 0.2 A cm_{geo}^{-2} to obtain χ_{OER} and χ_{COR}. The cell reversal experiments were conducted at 0.2 A cm_{geo}^{-2}, 80 °C cell temperature, RH of 100% for the supplied gases, 150/150 $kPa_{abs,inlet}$ total pressures and 1000/5000 nccm constant flow rates for the anode and cathode, respectively.

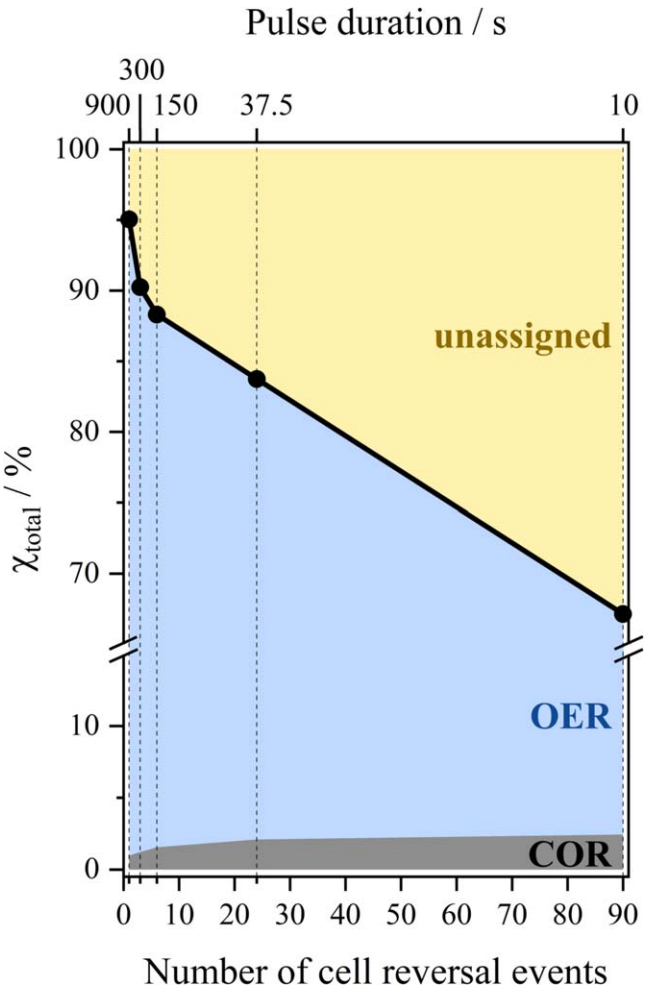

Figure 4. Total current efficiency (χ_{OER}) over the number of cell reversal events (n_{CR}) after an accumulated cell reversal time (t_{accum}) of 900 s. The sum (black line) of the current contributions from oxygen evolution reaction (OER: blue) and carbon corrosion reaction (COR: gray) are depicted. n_{CR} were derived from Eq. 3 for the correspondig pulse durations (t_{pulse}) (upper *x*-axis). The cell reversal experiments were conducted at 0.2 A cm^{-2}_{geo}, 80 °C cell temperature, RH of 100% for the supplied gases, 150/150 $kPa_{abs,inlet}$ total pressures and 1000/5000 nccm constant flow rates for the anode and cathode, respectively.

observable in the mass spectra (not shown here). In addition, an about 20–100 mV lower peak anode potential (Fig. S3b) for the shortest $t_{pulse} = 10$ and 37.5 s confirmed the residual H_2, i.e. a mixed potential. Considering the remaining H_2 in the cell, we assume an underestimation of the measured O_2 quantity due to a direct reaction of residual H_2 with the developed O_2 to form water and heat in the presence of a Pt-catalyst. Since the number of gas exchanges is relatively low for the AST protocols with longer $t_{pulse} = 150$, 300 and 900 s, the residual H_2 is less relevant. Notably, such an effect for the measured CO_2 quantity at very low t_{pulse} was not observed.

Assuming Faraday's law and a 4-electron process (acc. to Eqs. 1 and 2), the current efficiencies for the oxygen evolution reaction (χ_{OER}) and carbon oxidation reaction (χ_{COR}) were calculated with respect to the externally applied current of 0.2 A cm^{-2}_{geo}. Figure 3c shows the calculated current efficiencies as a function of t_{pulse} for $t_{accum} = 900$ s. Dependent on the cell reversal pulse duration, 1% to 2.5% of the externally supplied current (0.2 A cm^{-2}_{geo}) was consumed for carbon corrosion. By contrast, 65 to 95% were used for the electrolysis of water. Considering our quasi-continuous cell reversal experiment with $t_{pulse} = 900$ s, these current efficiencies are in good agreement with the results of Lim et al.[14] obtained for anode catalyst layers containing > 10 wt% IrO_2 as an water oxidation-enhancing catalyst. A clear trend depending on the pulse duration is observed. With decreasing t_{pulse} the carbon oxidation reaction part (Eq. 2) increases, most likely due to a Pt-catalyzed reaction pathway during sharply changing anode potentials[6,47,48] and/or by re-initiating the carbon corrosion process by the reduction of oxygen-based functional groups on the passivated carbon at potentials lower than 0.24 V_{RHE}[49] (see explanation above).

Figure 4 shows how the sum of the two faradaic charge components (black line), derived from on-line product analyses of the OER (blue area) and of the COR (gray area), compare to the actual faradaic charge as a function of number of cell reversals (bottom *x* axis), or equivalently, as function of the pulse duration (top *x* axis). The two charge/current components are plotted as a fractions of the total applied charge/current resulting in current efficiencies. The number of cell reversal events was derived from Eq. 3 for each t_{pulse} and a $t_{accum} = 900$ s. The fraction of the faradaic current that can be account for by OER and COR declined with rising number of individual cell reversal event, i.e. decreasing t_{pulse}, while the unassigned contribution (yellow area) to the total current grows. Initially, the drop is steeper for the lowest $n_{CR} = 1$ and 3, but then decreases linearly with increasing n_{CR}, which is accompanied by sharp anode potential step changes from 0 to > 1.4 V_{RHE} (Fig. S3). We suspect that the oxidation of metallic Pt^0 to PtO_x, that is the surface oxide build-up on the catalyst particles, combined with the formation of oxygenated carbonaceous species remaining on the surface, as well as increasing capacitive contributions are the origin of the unassigned charge. Furthermore, the oxidation of residual H_2 gas in the anode catalyst layer after the sudden gas exchanges, in particular for short pulse durations, may consume a part of the externally applied current. Likewise, the reaction of residual H_2 with oxygen may result in an underestimation of the measured O_2 quantity. Also, the contribution of other degradation products such as CO, which could not be quantified, cannot be excluded. Finally, we cannot rule out the possibility of additional potential cycling-induced faradaic degradation processes at short cell reversal pulses, such as Pt-dissolution.[50–52]

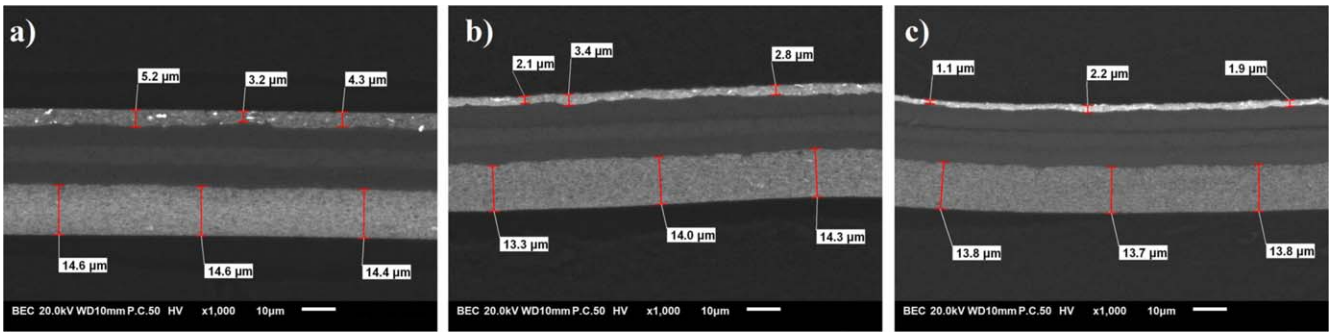

Figure 5. Representative cross-sectional SEM images of (a) fresh (BOL) and post-mortem MEAs (EOL: $t_{accum} = 900$ s) after the cell reversal experiment at (b) $t_{pulse} = 900$ s and (c) $t_{pulse} = 10$ s with the anode (top) and cathode (bottom) catalyst layer separated by a membrane (Gore M820.15, W. L. Gore & Associates, Inc.). Bright spots in anode catalyst layer are identified as IrO_2 particles by EDX analysis, not shown.

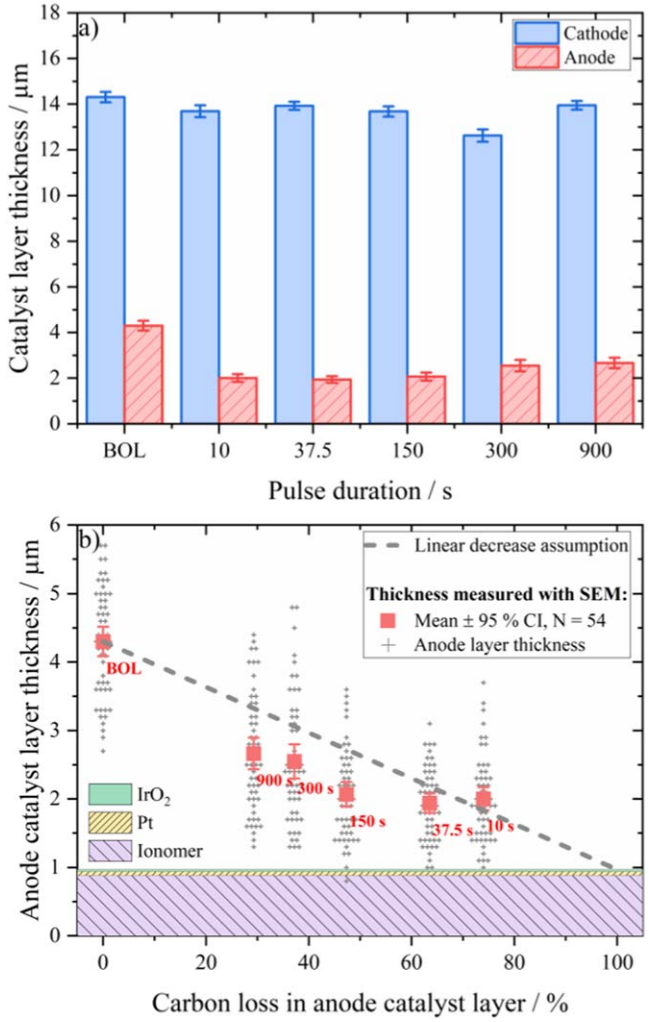

Figure 6. (a) Anode and cathode catalyst layer thicknesses for fresh (BOL) and post-mortem MEAs (EOL: t_{accum} = 900 s) after the cell reversal experiment at various t_{pulse}. (b) mean anode catalyst layer thicknesses (red squares) and the individual measuring points (gray crosses) from SEM thickness evaluation (*y*-axis) over the expected carbon loss from MS measurements (*x*-axis) of the anode catalyst layer for each sample (labelled with t_{pulse}). The depicted error bars represent the 95% confidence interval (CI) of the mean value of 54 individual measuring points via SEM. A calculated linear catalyst layer thickness decrease (gray dotted line) and a theoretical dense catalyst layer of about 1 μm thickness (colored and shaded region, consisting out of ionomer, Pt and IrO_2) at 100 wt% carbon support and porosity loss are plotted.

To assess the impact of carbon corrosion on the anode catalyst layer structure, thickness measurements of the catalyst layers was conducted using MEA cross-sections. In Fig. 5 representative cross-sectional SEM images are shown. Based on this analysis, the anode and cathode catalyst layer thicknesses are plotted in Fig. 6a for the fresh MEA (BOL) and post-mortem MEAs as a function of cell reversal pulse duration (each pulse duration is a separate MEA sample). No significant deviations in thicknesses of the MEA cutouts from inlet, middle and outlet region were found. Except for t_{pulse} = 300 s (cathode catalyst layer thickness of 12 μm), all cathode layer thicknesses ranged from 13−14 μm in line with the BOL MEA, suggesting no significant change in cathode catalyst layer thickness during the cell reversal experiments. Note that the MEA for t_{pulse} = 300 s experiments had a somewhat lower cathode Pt-loading, which is probably due to a thinner bar-coated layer in the initial state. By contrast, a significant decrease in the anode catalyst layer thickness was evident, from an initial value of 4.5 μm for the fresh MEA to 2.5–3 μm thickness for longer t_{pulse} and reaching the thinnest catalyst layers of $\leqslant$ 2 μm for the shortest t_{pulse} experiments. This confirms our previous conclusions of more severe degradation (see Fig. 3a) at shorter pulse intervals. In order to prove the origin of the CO_2 detected in the anode exhaust, the previously presented total amounts of measured CO_2 were taken to calculate the expected loss of carbon (Eq. 2) in the anode catalyst layer for each t_{pulse}, respectively. The calculated carbon loss with respect to the initial carbon content in the anode (ionomer excluded) ranged between 30 wt% for long pulses and 75 wt% for the shortest pulse. In Fig. 6b the experimental anode catalyst layer mean thicknesses (red squares) are compared to the expected carbon loss calculated from MS measurement, while the individual SEM measuring points are shown as gray cross symbols. Data labels denote the duration of a single fuel starvation pulse t_{pulse}. Under the assumption that the detected CO_2 largely originates from the oxidation of the anode carbon support and does not derive from the carbon-based ionomer, GDL, and flow field material, the expected decrease in anode catalyst layer thickness with progressing carbon corrosion can be predicted (dashed line in Fig. 6b). The following assumptions were made: (i) a simplified linear decrease in anode catalyst layer thickness with progressing carbon loss, (ii) a complete loss of the porosity at 100 wt % carbon loss, and (iii) a remaining dense anode catalyst layer of approx. 1 μm thickness only containing ionomer, platinum and IrO_2 (shaded colored areas in Fig. 6b) at 100% carbon support loss in anode catalyst layer. Note that the thickness of the dense anode catalyst layer was calculated by the loading (mg cm^{-2}_{geo}) of each individual component - which is accessible from the ink formulation - and assuming a density of 21.45 g cm^{-3} for Pt, 11.7 g cm^{-3} for IrO_2 and 2.1 g cm^{-3} for the ionomer. The expected linear trend line is in very good agreement with the actual SEM-measured layer thicknesses, supporting our assumptions. In contrast, other groups observed a larger reduction in thickness with less carbon loss, concluding a compaction and loss of porosity of their catalyst layer.[48] While these conflicting observations cannot be finally resolved by our present measurements, we suggest that the origin lies in distinct electrode structure, e.g. carbon type, electrode thickness, ionomer content. Note further that in Fig. 6b essentially no measured data point falls below the hypothesized dense catalyst layer thickness of approx. 1 μm, which confirms our assumptions *(ii) and (iii)* further. Our results suggest that the carbon-based support material inside the anode catalyst layer is preferably corroded compared to other carbon sources (GDL, flow field) at least in the so-called water electrolysis region $>$ −1.25 V overall cell voltage, where OER mainly takes place.[2] Although carbon corrosion, likely following a Pt-catalyzed carbon corrosion mechanism, appears to largely affect the carbon support, we cannot exclude that other carbon sources are oxidized at a low level, as well.[22] This may hold true in particular at later stages, when the carbon content in the anode catalyst layer has gradually depleted after frequent progressive cell reversal and the overall cell voltage falls below −1.25 V, that is at anode potentials $>$ 2.0 V_{RHE}.

To further investigate the origin of the performance loss, the CVs of the cathode and anode electrode were evaluated. An approximately 8% change in the cathode ECSA ($ECSA_{BOL}$: 59 ± 1 m^2_{Pt} g^{-1}_{Pt} vs $ECSA_{EOL}$: 54 ± 1 m^2_{Pt} g^{-1}_{Pt}, not shown) was observed, independent of the applied cell reversal protocol. At the anode, the interim and end of life (EOL) CV patterns differed sharply from the beginning of life (BOL) CVs. They exhibited distinct characteristics that depended on the number and type of performed cell reversal protocol and thus the progress of degradation. Note that CO contaminants on Platinum were removed during the first CV cycle, as previously investigated elsewhere.[5] In Fig. 7, representative CVs of the anode electrode of two fresh MEAs (BOL, solid lines) and the corresponding end of life (EOL, t_{accum} = 900 s, dotted lines) CVs of the shortest t_{pulse} = 10 s (black) and the longest t_{pulse} = 900 s (green) samples are shown. All anode CVs feature the typical underpotential hydrogen desorption/adsorption (upd) peaks in the range of 0.1–0.4 V_{RHE} range and Pt surface oxidation/reduction

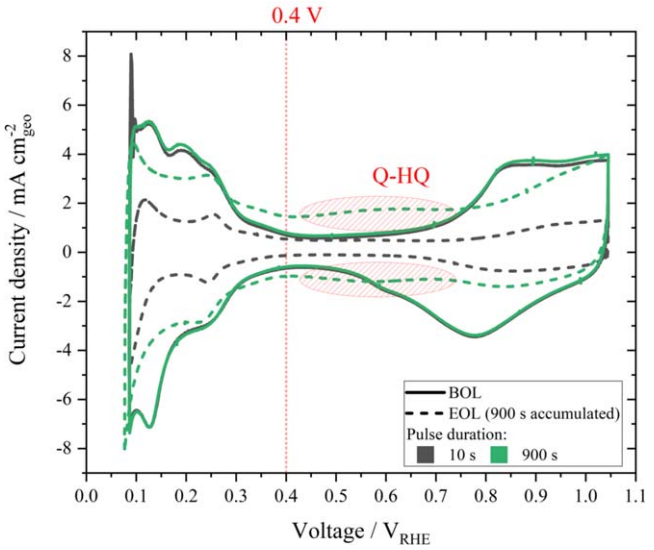

Figure 7. Cyclic voltammogram (CV) of the anode electrode. Beginning of life (BOL, solid line) and end of life (EOL, dotted line) with 900 s accumulated cell reversal time for t_{pulse} = 10 s (black color) and t_{pulse} = 900 s (green color). CVs: scan rate of 50 mV s^{-1} in MEA configuration at 35 °C cell temperature, RH of 100%, 50 nccm N_2 to the anode and 1000 nccm diluted H_2 (3 % in Ar) to the cathode at ambient pressures. Note that the voltage is corrected by the thermodynamical shift with respect to 100 $kPa_{abs,inlet}$ H_2 (approx. 47 mV for 3% H_2 at 35 °C). The shaded regions indicate the formation of quinone/hydroquinone redox peaks (Q-HQ) in the voltammograms. The red line shows the voltage at which the double layer charge is determined.

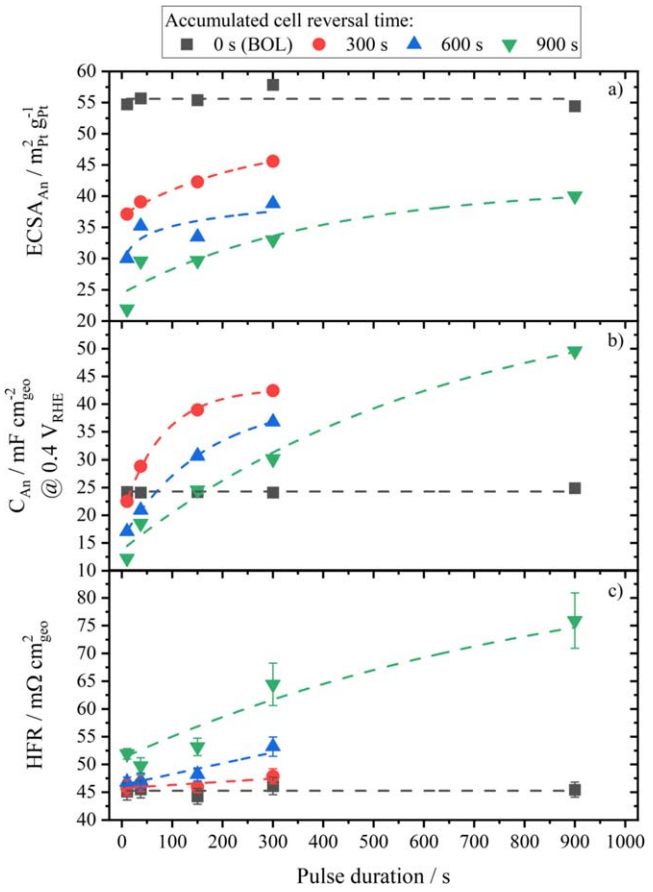

Figure 8. Various characteristic parameters in dependence of the accumulated cell reversal time (BOL: black squares, 0–300 s: red circles, 0–600 s: blue triangles, 0–900 s: green upside down triangles) versus applied pulse duration. (a) Electrochemically active surface area of the anode, ECSA, calculated from the H_{upd} area and (b) corresponding capacitance of the anode, C, at 0.4 V_{RHE}. Cyclic voltammogram: scan rate 50 mV s^{-1} in MEA configuration at 35 °C cell temperature, RH of 100%, 50 nccm N_2 to the anode and 1000 nccm diluted H_2 (3 % in Ar) to the cathode at ambient pressures. (c) High frequency resistance, HFR, determined at each DC current step of the polarization curve utilizing the electrochemical impedance spectroscopy (EIS) in pseudo-galvanostatic mode within a frequency range of 100 kHz - 0.01 Hz and an AC perturbation of 4 mV_{rms}. Error bars show the absolute range of the HFR in dependence of the DC current at which the HFR was determined, with the highest HFR values belonging to the lowest DC currents, and vice versa. Conditions were adjusted to 80 °C with fully humidified H_2/Air (RH = 100%), differential flow rates of 1000/5000 nccm and a pressure of 150 $kPa_{abs,inlet}$ at both electrodes.

peaks between 0.6–1.0 V_{RHE}.[36] Here, already the effect of the degradation can be identified by the intensity and shape of the respective features. Compared to the BOL CV, the short-pulsed sample exhibited a diminished double layer region between 0.4–0.6 V_{RHE}, validating the loss of carbon support material due to its oxidation and further gasification to CO_2 during several cell reversal events. In contrast, the double layer region for the long t_{pulse} sample drastically expanded with an additional peak showing up at about 0.6 V_{RHE}. Previously, Mandal et al.[3] found a similar evolution of a new peak at about 0.55 V_{RHE} corresponding to the quinone-hydroquinone (Q-HQ) redox couple for their continuous-like (600 s) cell reversal investigations. During their 1.2 V potential hold experiments under PEMFC relevant conditions Kangasniemi et al.[4] made the observations that the electroactive Q-HQ peak is an indicator for the formation of various oxygen-based functional groups on the carbon support, e.g. carbonyl (>C=O), carboxyl (–COOH), hydroxyl (–OH) and other. A probable impact of these surface oxide groups on the electrical properties of the carbon support will be discussed in detail in the following sections (see Figs. 8c and 9).

In Fig. 8a the ECSA of the anode electrode is plotted against t_{pulse} at varying t_{accum}. The BOL ECSAs (black squares) for all samples are close to each other (56 ± 2 m^2_{Pt} g^{-1}_{Pt}) which underline the reproducibility of electrode preparation. With progressing cell reversal time, the ECSA decreases more severely for short t_{pulse} = 10 s pulsed cell reversal protocols than for long t_{pulse} = 900 s, e.g. a decrease to 22 m^2_{Pt} g^{-1}_{Pt} compared to 40 m^2_{Pt} g^{-1}_{Pt} for 900 s accumulated cell reversal time. This about 2.2-fold higher decrease in ECSA of the anode electrode fit well with the mass spectroscopy data above, considering the approx. 2.5-fold higher CO_2 evolution rate for short-pulsed compared to long-pulsed cell reversal tests (see Fig. 3a). This consistency suggests that the detachment of Pt particles due to the corrosion of the carbon support is a major contributor to the loss of ECSA, without excluding other degradation mechanisms, e.g. Pt dissolution,[52] Ostwald ripening, particle coalescence, which was not investigated in this work. Assuming linear kinetics for the HOR[53,54] and an exchange current density $i_{0,HOR}$ of 200[55]–600[54] mA cm^{-2}_{Pt} at the chosen conditions (80 °C and 150 $kPa_{abs,inlet}$), the ECSA loss to 22 m^2_{Pt} g^{-1}_{Pt} would cause only a negligible kinetic loss of 1–4 mV at 1.0 A cm^{-2}_{geo} for a Pt-loading of 0.1 mg_{Pt} cm^{-2}_{geo}. However, at lower anode loadings and considering possible catalyst poisoning due to H_2-gas impurities (e.g. CO),[2,56] say if reformed H_2 would be used in the application, this degradation would have a significant effect on the overall performance.

Figure 8b shows the capacitance at 0.4 V_{RHE} - comprising the capacitive current at 0.4 V_{RHE} divided by the scan rate of 50 mV s^{-1} - as a function of t_{pulse} at progressing t_{accum}. The BOL capacitance (black squares) was determined to be 24.5 ± 0.5 mF cm^{-2}_{geo} for all fresh samples. An immediate and gradual decrease in capacitance was observed for the short-pulsed sample to 50% of its initial value after t_{accum} = 900 s. The samples treated with t_{pulse} = 37.5–300 s exhibited an initial increase in capacitance at t_{accum} = 300 s, which was followed by a gradual decrease with progressive cell reversal

times. Interestingly, the EOL capacitance for the t_{pulse} = 900 s sample is twice that of the t_{pulse} = 10 s sample, pointing to the highest surface oxide build-up on carbon during long-lasting voltages of > 1.5 V_{RHE} potentials (s. supplemental material, anode potential). Since different processes occur simultaneously, which change the surface and the content of the carbon support inside the anode catalyst layer, various phenomena need to be taken into consideration for an interpretation of the data. Long potential holds favor the formation of surface oxides, indicated by the appearance of a Q-HQ peak and thus, may increase the capacitive response due to a hydrophilicity change.[4] In contrast, short pulsed cell reversal events and interim steps in normal (H_2/Air) operation seemingly suppress and/or recover the formation of surface oxides. A carbon loss due to progressive carbon corrosion to CO_x and/or an associated deactivation of partial electrode areas due to loss of electrical connection, on the other hand, decreases the capacitive response and is more pronounced for the short-pulsed samples. Concurrently, carbon support corrosion may also cause a surface roughening which in turn would increase the double layer capacity.

To investigate the structural changes during accelerated stress test protocols further, Fig. 8c shows the high frequency resistance (HFR) as a function of pulse duration (t_{pulse}) for various accumulated cell reversal time. The HFR represents the ohmic resistance of the MEA, which is the sum of contact resistances and bulk resistances of the components, e.g. electronic resistances of the catalyst layer, GDL and flow field as well as the protonic resistance of the membrane.[41] Contrary to the measured CO_2 evolution, which increases with decreasing t_{pulse} (see Fig. 3a), the HFR raises significantly with longer t_{pulse}. While the growth of the HFR is only 15% of its initial value of 45 ± 1 mΩ cm^2_{geo} (black squares) for t_{pulse} = 10 s, it increased by almost 80% for the longest pulse duration of t_{pulse} = 900 s. Applying Ohm's law, the almost 65% higher HFR increase would cause an additional voltage loss of about 30 mV at 1.0 A cm^{-2}_{geo}, which is in good agreement with the additional voltage loss of 40 mV observed in the polarization curves (cf. Table I), when comparing the short-pulsed with the long-pulsed samples. Notably, the error bars in Fig. 8c show the dependence of the HFR on the current density, where it was determined. Generally, the dependence is low for humidified test conditions, as seen in the BOL values (black squares). However, for the degraded samples (300 and 900 s EOL) the HFR showed a stronger dependence on the current density and thus on the water content inside the MEA. This confirms the altered surface properties, e.g. hydrophilicity,[4] of the carbon support due to the formation of surface oxides and raises concerns to the water management inside the catalyst layer, as other groups revealed for cathodes after accelerated stress test protocols.[57] The loss of hydrophobic character of the carbon support on the anode as well as minor activity losses on the cathode side (about 8% ECSA loss) are assumed to be the origin of the remaining residual voltage loss of about 40–50 mV, which could not be explained with the anode-side ECSA loss and HFR increase in our study.

A recent state-of-the-art review on understanding and tuning the electrical properties of amorphous carbons confirmed the detrimental influence of oxygen-containing surface functional groups on the electrical conductivity. Although several physicochemical models were postulated, it remained unclear in which way the chemisorption of electronegative oxygen at the edges of nanocrystalline graphite clusters diminishes the electronic conduction.[58] To better illustrate the possible role of surface oxides as possible origin of the increased HFR of the long-pulsed samples (see Fig. 8c), two possible degradation mechanisms are visualized in Fig. 9. On the left-hand side a pristine catalyst agglomerate is shown with multiple intact contact areas between each single carbon particle. During fuel starvation conditions, the high anode potential leads, on the one hand, to a corrosion of the carbon-based support material (Fig. 9, I). This decreases the contact area between individual carbon particles inside the catalyst layer as well as the contact surface to adjacent

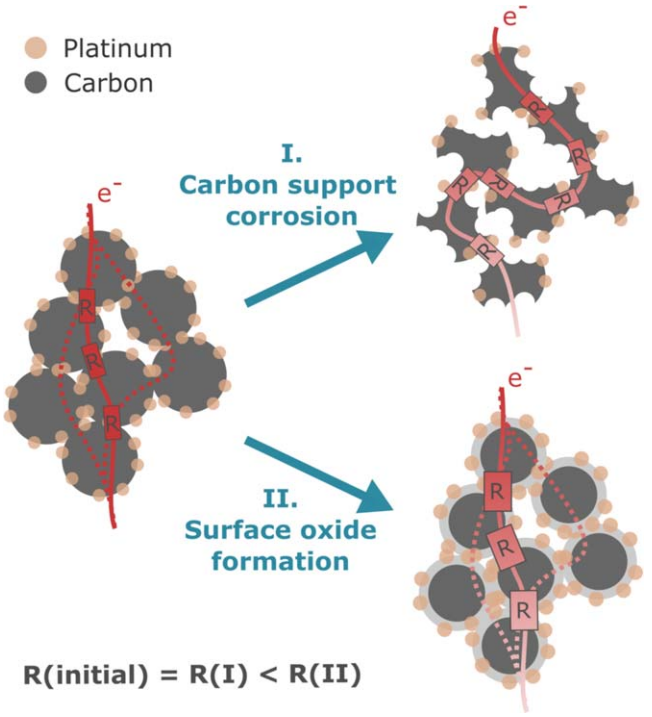

Figure 9. Schematic representation of the suggested degradation mechanisms occuring during fuel starvation events. Left-hand side: a pristine carbon-supported catalyst agglomerate (carbon: gray, platinum: beige) with several intact electron pathways (red lines) and contact resistances. Upper right corner: a corroded carbon-supported catalyst agglomerate (I) with narrowed electron pathways and damaged contact areas, bottom right corner: an intrinsic resistance increase due to surface oxide build-up (II).

layers, i.e. the gas diffusion layer. As a result, previously possible electron pathways shrink or disappear and the intraparticle resistance increases. On the other hand, the high anode potentials lead to a formation of oxygen-based functional groups on the carbon surface (Fig. 9, II). This is accompanied by a decline or disruption of the intrinsic electronic conductivity[58] and consequently the ohmic resistance rises. While competing in electron consumption, both degradation mechanisms are likely to occur simultaneously, albeit to a different extent depending on the design of the cell reversal test protocol. This simultaneity is further strengthened by considering the formed surface oxides as a reaction intermediate for its further gasification to CO_2.[48] Short fuel starvation pulses with recovery phases in between promote a higher carbon corrosion, while the surface oxide build-up is limited due to short exposure times and a partial or full recovery within the normal operation phases. In contrast, for protocols with long fuel starvation pulses, the carbon corrosion rate more than halved, whereas the surface oxide formation is considerably higher, as confirmed by the appearance of Q-HQ peaks and the higher double layer capacitance (cf. Fig. 7). As stated previously, the higher build-up of surface oxides is identified to have a greater contribution to the overall performance loss by increasing the HFR to a much higher level (see Fig. 8c). Note that the assumption was made that the membrane resistance did not change due to our cell reversal experiments. Further investigations on the removal of the formed surface oxides on carbon and thus, on the reversibility of the increase in ohmic resistance will be conducted in near future.

Conclusions

In this study, we systematically investigated the design of different accelerated stress test protocols to simulate cell reversal

events in PEM fuel cells under operation conditions ranging from short pulsed to continuous-like fuel starvation events, while keeping the accumulated cell reversal time constant. We applied these protocols to fuel cells with reversal-tolerant anodes, and found 2.5-fold higher carbon corrosion currents if the duration of the applied pulsed fuel starvation event was reduced from 900 s to 10 s. Shortening the pulse duration was accompanied by an approximately 2.2-fold higher ECSA loss on the anode electrode, whereas the ECSA of the cathode electrode was nearly unaffected (8% loss). Moreover, a decreased carbon corrosion on aged Pt/C catalysts was observed. These findings are in good agreement with the results of other groups,[6,47,48] investigating Pt/C-catalysts behavior under constant voltage compared to potentiodynamic operation. Furthermore, our combined exhaust gas analysis using mass spectroscopy technique and SEM electrode thickness results demonstrated that the carbon-based support material within the catalyst layer is preferably corroded over other carbon sources, e.g. carbon-based GDL and flow field materials, at least during early phases of cell reversal event in the so-called water electrolysis region (> -1.25 V).

However, looking at the ohmic resistance (represented by the high frequency resistance, HFR) a reverse observation was made, with an almost 80% growth (relative to the HFR of a fresh MEA) in ohmic resistance for the long 900 s pulse protocol compared to a mere 15% rise for the short 10 s pulsed protocol. In this regard, two possible degradation mechanisms for the increase in ohmic resistance were suggested: First, an intraparticle resistance increase due to carbon support corrosion and, on the other hand, a decrease of intrinsic electron conductivity due to the build-up of oxygen-based functional groups on the carbon support surface. We assigned the carbon surface oxidation as the main contributor to the HFR increase for the anodes continuously situated under high potentials due to long fuel starvation events and confirmed the presence of oxygen-based functional groups with a rising quinone-hydroquinone redox couple at approximately 0.6 V_{RHE} in anode cyclic voltammograms. Further studies will be conducted on the reversibility of the formed oxygen-based functional groups under anode relevant conditions.

The opposite observations - a higher carbon corrosion rate for short pulsed protocols, but a higher surface oxide build-up for long fuel starvation events - demonstrate that more understanding on the application-relevant conditions are necessary in order to define representative test protocols and to develop suitable reversal tolerant materials. With regard to the specific application and a harmonization of testing, we suggest utilizing pulsed test protocols if system mitigation strategies are incorporated, and continuous protocols if no system remedies are available to minimize the time under fuel starvation conditions.

Acknowledgments

Colleagues at Heraeus Deutschland GmbH & Co. KG, Global Business Unit Heraeus Precious Metals, Department Hydrogen Systems are gratefully acknowledged for many fruitful discussions.

ORCID

Robert Marić https://orcid.org/0000-0003-4107-7461
Frédéric Hasché https://orcid.org/0000-0002-9353-0603
Peter Strasser https://orcid.org/0000-0002-3884-436X

References

1. R. Borup et al., *Chem. Rev.*, **107**, 3904 (2007).
2. T. Ralph and M. Hogarth, *Platinum Met. Rev.*, **46**, 117 (2002), https://www.technology.matthey.com/wp-content/uploads/pdf/pmr-v46-i3-117-135.pdf.
3. P. Mandal, B. K. Hong, J. G. Oh, and S. Litster, *J. Power Sources*, **397**, 397 (2018).
4. K. H. Kangasniemi, D. A. Condit, and T. D. Jarvi, *J. Electrochem. Soc.*, **151**, E125 (2004).
5. J. Kang, D. W. Jung, S. Park, J. H. Lee, J. Ko, and J. Kim, *Int. J. Hydrogen Energy*, **35**, 3727 (2010).
6. S. Maass, F. Finsterwalder, G. Frank, R. Hartmann, and C. Merten, *J. Power Sources*, **176**, 444 (2008).
7. A. Taniguchi, T. Akita, K. Yasuda, and Y. Miyazaki, *J. Power Sources*, **130**, 42 (2004).
8. T. Ioroi and K. Yasuda, *J. Power Sources*, **450**, 227656 (2020).
9. J. Zhang, *PEM Fuel Cell Electrocatalysts and Catalyst Layers: Fundamentals and applications* (Springer-Verlag London Limited, London) p. 835 (2008).
10. W. R. Baumgartner, P. Parz, S. D. Fraser, E. Wallnöfer, and V. Hacker, *J. Power Sources*, **182**, 413 (2008).
11. W. R. Baumgartner, E. Wallnöfer, T. Schaffer, J. O. Besenhard, V. Hacker, V. Peinecke, and P. Prenninger, *ECS Trans.*, **3**, 811 (2006).
12. H.-L. Chang and J.-L. Huang, *Fuel cell voltage measurement device*, US7639023B2 (2009).
13. W. R. Daud, R. E. Rosli, E. H. Majlan, S. A. Hamid, R. Mohamed, and T. Husaini, *Renewable Energy*, **113**, 620 (2017).
14. K. H. Lim, W. H. Lee, Y. Jeong, and H. Kim, *J. Electrochem. Soc.*, **164**, F1580 (2017).
15. B. K. Hong, P. Mandal, J. G. Oh, and S. Litster, *J. Power Sources*, **328**, 280 (2016).
16. S. D. Knights, D. P. Wilkinson, S. A. Cambell, J. L. Taylor, J. M. Gascoyne, and T. R. Ralph, *Fuel cell anode structure for voltage reversal tolerance*, WO2001015247A2 (2001).
17. F. Bizzotto, J. Quinson, A. Zana, J. J. K. Kirkensgaard, A. Dworzak, M. Oezaslan, and M. Arenz, *Catal. Sci. Technol.*, **9**, 6345 (2019).
18. T. Reier, M. Oezaslan, and P. Strasser, *ACS Catal.*, **2**, 1765 (2012).
19. T. Reier, D. Teschner, T. Lunkenbein, A. Bergmann, S. Selve, R. Kraehnert, R. Schloegl, and P. Strasser, *J. Electrochem. Soc.*, **161**, F876 (2014).
20. E. You, M. Min, S.-A. Jin, T. Kim, and C. Pak, *J. Electrochem. Soc.*, **165**, F3094 (2018).
21. C. Pak, S. W. Lee, C. Baik, B. H. Lee, D. J. You, and E. You, *Chin. Chem. Lett.*, **30**, 1186 (2019).
22. S. W. Lee, B. H. Lee, T. Y. Kim, C. Baik, M. S. Kim, G. S. Chai, and C. Pak, *Catal. Commun.*, **130**, 105758 (2019).
23. H. Schmies et al., *Chem. Mater.*, **30**, 7287 (2018).
24. S. Henning, R. Shimizu, J. Herranz, L. Kühn, A. Eychmüller, M. Uchida, K. Kakinuma, and T. J. Schmidt, *J. Electrochem. Soc.*, **165**, F3001 (2018).
25. H. Schmies et al., *Adv. Energy Mater.*, **8**, 1701663 (2018).
26. E. Hornberger et al., *ACS Catal.*, **8**, 9675 (2018).
27. I. C. Halalay, S. Swathirajan, B. Merzougui, M. P. Balogh, G. C. Garabedian, and M. K. Carpenter, *J. Electrochem. Soc.*, **158**, B313 (2011).
28. J. Zhang, H. A. Gasteiger, W. Gu, P. T. Yu, and J. E. O'Hara, *Using Sacrificial Material To Mitigate Catalyst Support Corrosion In Fuel Cell Electrode*, US20080020262A1 (2008).
29. S. D. Knights, K. M. Colbow, J. St-Pierre, and D. P. Wilkinson, *J. Power Sources*, **127**, 127 (2004).
30. P. Mandal, B. K. Hong, J.-G. Oh, and S. Litster, *ECS Trans.*, **69**, 443 (2015).
31. L. Hu, B. K. Hong, J. G. Oh, and S. Litster, *ECS Trans.*, **80**, 535 (2017).
32. D. Liang, Q. Shen, M. Hou, Z. Shao, and B. Yi, *J. Power Sources*, **194**, 847 (2009).
33. D. Liang, M. Dou, M. Hou, Q. Shen, Z. Shao, and B. Yi, *J. Power Sources*, **196**, 5595 (2011).
34. T. R. Ralph, S. Hudson, and D. P. Wilkinson, *ECS Trans.*, **1**, 67 (2006).
35. Z. Zhu, X. Yan, H. Tang, H. Cai, M. Pan, H. Zhang, and J. Luo, *J. Power Sources*, **351**, 138 (2017).
36. S. S. Kocha, "Principles of MEA preparation." *Handbook of Fuel Cells* 3, ed. W. Vielstich, H. Yokokawa, and H. A. Gasteiger (Wiley, Chichester) p. 538 (2003).
37. D. R. Baker, D. A. Caulk, K. C. Neyerlin, and M. W. Murphy, *J. Electrochem. Soc.*, **156**, B991 (2009).
38. T. Mittermeier, A. Weiß, F. Hasché, and H. A. Gasteiger, *J. Electrochem. Soc.*, **165**, F1349 (2018).
39. X. Z. Yuan, H. Wang, J. Colin Sun, and J. Zhang, *Int. J. Hydrogen Energy*, **32**, 4365 (2007).
40. R. N. Carter, S. S. Kocha, F. Wagner, M. Fay, and H. A. Gasteiger, *ECS Trans.*, **11**, 403 (2007).
41. H. A. Gasteiger, W. Gu, R. Makharia, M. F. Mathias, and B. Sompalli, "Beginning-of-life MEA performance - Efficiency loss contributions." *Handbook of Fuel Cells* 3, ed. W. Vielstich, H. Yokokawa, and H. A. Gasteiger (Wiley, Chichester) p. 593 (2003).
42. R. Makharia, S. S. Kocha, P. T. Yu, M. A. Sweikart, W. Gu, F. T. Wagner, and H. A. Gasteiger, *ECS Trans.*, **1**, 3 (2006).
43. S. B. Adler, *J. Electrochem. Soc.*, **149**, E166 (2002).
44. W. He and T. V. Nguyen, *J. Electrochem. Soc.*, **151**, A185 (2004).
45. M. Kim, N. Jung, K. Eom, S. J. Yoo, J. Y. Kim, J. H. Jang, H. J. Kim, B. K. Hong, and E. Cho, *J. Power Sources*, **266**, 332 (2014).
46. T. Mittermeier, A. Weiß, F. Hasché, G. Hübner, and H. A. Gasteiger, *J. Electrochem. Soc.*, **164**, F127 (2017).
47. N. Linse, L. Gubler, G. G. Scherer, and A. Wokaun, *Electrochim. Acta*, **56**, 7541 (2011).
48. N. Macauley, D. D. Papadias, J. Fairweather, D. Spernjak, D. Langlois, R. Ahluwalia, K. L. More, R. Mukundan, and R. L. Borup, *J. Electrochem. Soc.*, **165**, 3148 (2018).
49. S. J. Ashton and M. Arenz, *Electrochem. Commun.*, **13**, 1473 (2011).
50. A. A. Topalov, S. Cherevko, A. R. Zeradjanin, J. C. Meier, I. Katsounaros, and K. J. Mayrhofer, *Chem. Sci.*, **5**, 631 (2014).
51. C. Gebauer, Z. Jusys, and R. J. Behm, *J. Electrochem. Soc.*, **165**, J3342 (2018).
52. A. A. Topalov, I. Katsounaros, M. Auinger, S. Cherevko, J. C Meier, S. O. Klemm, and K. J. Mayrhofer, *Angew. Chem. - Int. Ed.*, **51**, 12613 (2012).

53. W. Gu, D. R. Baker, Y. Liu, and H. A. Gasteiger, "Proton exchange membrane fuel cell (PEMFC) down-the-channel performance model." *Handbook of Fuel Cells* 6, ed. W. Vielstich, H. Yokokawa, and H. A. Gasteiger (Wiley, Chichester) p. 631 (2009).
54. K. C. Neyerlin, W. Gu, J. Jorne, and H. A. Gasteiger, *J. Electrochem. Soc.*, **154**, B631 (2007).
55. J. Durst, C. Simon, F. Hasche, and H. A. Gasteiger, *J. Electrochem. Soc.*, **162**, F190 (2015).
56. V. M. Schmidt, H.-f. Oetjen, and J. Divisek, *J. Electrochem. Soc.*, **144**, L237 (1997).
57. X. Zhang, L. Guo, and H. Liu, *J. Power Sources*, **296**, 327 (2015).
58. A. B. Bogeat, *Crit. Rev. Solid State Mater. Sci.* (2019).